

1 Provenance of block fields along lunar wrinkle ridges

2 Renee A. French^{a,b,c}, Thomas R. Watters^{d*}, Mark S. Robinson^e

3 ^aNorthwestern University, Department of Earth and Planetary Sciences, 2145 Sheridan Rd,
4 Evanston, Illinois, 60208-3130, USA.

5 ^b Present address: Oakton Community College, Division of STEM and Health Careers, Des
6 Plaines Campus, 1600 E. Golf Road, Des Plaines, IL, 60016

7 ^c Present address: Harold Washington College, Department of Physical Sciences, 30 E.
8 Lake St, Chicago, IL, 60601

9 ^d Smithsonian Institute, National Air and Space Museum, Center for Earth and Planetary
10 Studies, Washington, D.C., 20013, USA.

11 ^e Arizona State University, School of Earth and Space Exploration, Tempe, Arizona,
12 85287, USA.

13 *Corresponding author: watterst@si.edu, +1 (202) 633-2483

14 **Keywords**

15 Moon; Moon, surface; Tectonics; Geological processes

16 **Highlights**

- 17 • Blocky wrinkle ridges are roughly evenly distributed throughout the maria, and
18 block density generally increases with slope
- 19 • Blocks are likely formed by deformation of mare basalts during wrinkle ridge
20 formation
- 21 • Block size and high reflectance material in block fields suggest activity within the
22 last 300 Ma

October 11, 2019

23 **Abstract**

24 Block fields and associated relatively high reflectance material along wrinkle ridge
25 summits are revealed in meter scale Lunar Reconnaissance Orbiter Camera (LROC)
26 images. Wrinkle ridges with block fields in Mare Australe, Crisium, Fecunditatis, Frigoris,
27 Nubium, the northern half of Oceanus Procellarum, Serenitatis, and Tranquillitatis are
28 evenly distributed, and block density generally increases with wrinkle ridge slope. The
29 median cross-sectional area (proxy for diameter) of the 1,368 blocks measured in this study
30 is $\sim 7 \text{ m}^2$ and 75% of these blocks are $\leq \sim 14 \text{ m}^2$. We propose that the largest variation
31 in cross-sectional area of the blocks is related to substrate physical properties of the mare
32 basalt and not a function of the slope on which they occur, suggesting that physical
33 properties rather than slope is a stronger control on block size. The maximum length of
34 blocks may constrain the minimum basalt flow thickness or joint width; our block
35 measurements suggest basalt flows $\sim 2 - 14 \text{ m}$ thick, agreeing with previous estimates. The
36 data suggest that blocks originate from mare basalt layers that buckle and break as a result
37 of movement along ridge-forming thrust faults. High reflectance material associated with
38 wrinkle ridge blocks likely represents freshly exposed rock and soil. Meter-scale blocks
39 may erode relatively quickly due to collisional disruption, indicating recent down-slope
40 movement of regolith exposing preexisting blocks, or blocks formed and exposed by recent
41 activity on ridge-forming faults.

42

43

44

45 **1. Introduction**

46 Wrinkle ridges are one of the most common tectonic landforms on the terrestrial
47 planets [Watters, 1988]. They are complex landforms often composed of broad, low relief
48 arches and narrow, asymmetric superimposed ridges (Fig. 1). The broad arch is often only
49 discernable in high incidence (Sun low to the horizon) angle photographs and images. The
50 superimposed ridge is usually relatively narrow and strongly asymmetric in cross-section.
51 Wrinkle ridges are the result of contractional deformation and are the expression of both
52 folding and thrust faulting [Plescia and Golombek, 1986; Watters, 1988; Schultz, 2000].

53 Localized block fields associated with mare wrinkle ridges were first discovered in
54 the Lunar Reconnaissance Orbiter mission in Lunar Reconnaissance Orbiter Camera
55 (LROC) Narrow Angle Camera (NAC) meter-scale images. Block fields have been found
56 along many mare wrinkle ridges, but do not occur along the entire length of a ridge (Figure
57 1, 2). Block fields co-located with relatively high reflectance material (typically 5-10%
58 higher but can be as high as ~25%) are observed along the slopes of many wrinkle ridges.
59 Fields vary in size up to 100 m in the short dimension and up to several kilometers in
60 length.

61 Since their discovery, the distribution, spatial characteristics and origin of wrinkle
62 ridge block fields have not been investigated in detail. The high reflectance material
63 typically found with wrinkle ridge blocks likely represents freshly exposed rock and soil.
64 Alternatively, the albedo contrast may be due to a compositional difference and not a
65 contrast in maturity. However, since we have no evidence to support a compositional
66 difference, we interpret the contrast in reflectance to be the result of maturity.

67 We consider three competing hypotheses for the formation of these block fields:
68 the blocks and high reflectance material either (1) originated elsewhere and were
69 transported to their current location (e.g., impact ejecta), (2) were present before
70 deformation and ridge formation, or (3) are disrupted bedrock being exposed and eroded.
71 To test these hypotheses, we characterize the morphometry and distribution of blocky
72 wrinkle ridges in Mare Australe, Crisium, Fecunditatis, Frigoris, Nubium, the northern half
73 of Oceanus Procellarum, Serenitatis, and Tranquillitatis. These regions have at least one
74 LROC Narrow Angle Camera (NAC) stereo pair covering the block field, allowing for a
75 detailed analysis of block density and size as a function of slope for 10 wrinkle ridges.
76 Trends within and between maria are discussed, and trends in block size are used to infer
77 flow thicknesses or joint widths.

78 **2. Methods**

79 LROC Quickmap (<http://target.lroc.asu.edu/q3/>) was used for visual classification
80 of wrinkle ridges (i.e., blocky, non-blocky, or unclassified) and wrinkle ridges were
81 mapped using ArcGIS. Wrinkle ridges are classified as ‘unclassified’ if there was not
82 adequate high resolution imagery with adequate lighting conditions (incidence angles
83 greater than 50°) to determine the presence of blocks. Quickmap was used to select LROC
84 NAC images for specific wrinkle ridges, which were then processed using the Integrated
85 System for Imagers and Spectrometers (ISIS) (Anderson et al., 2004), and slope data were
86 obtained from digital elevation models (DEMs) derived from NAC stereo pairs using
87 SOCET SET (precision error ranging from 0.7 – 4.5 m; Henriksen et al., 2016). For this
88 study, we analyzed DEMs along ridges in Maria Australe, Crisium, Frigoris, Nubium,

89 Serenitatis, and Tranquillitatis, and DEMs for two ridges in both Mare Fecunditatis and
90 northern Oceanus Procellarum (hereafter referred to as North Procellarum) for a total of 10
91 ridges (and thus 10 DEMs). Elevations (spatial resolution ranging from 2 – 7 m) were
92 converted to slopes using the *Slope* tool in ArcMap. The sizes of relatively crisp and
93 cohesive blocks were determined using the *qview Measure* tool in ISIS. Blocks were
94 counted using *qview* to determine the spatial density. Counts were made in rectangular
95 sample areas of 10,000 m². Block density measurements were concentrated along wrinkle
96 ridge crests and block counts were assigned to maximum slopes within these areas (e.g.,
97 blocks that were counted in an area with a maximum slope of 20 degrees were assigned to
98 the 15 degree bin). Block shapes were approximated by and measured as ellipses, resulting
99 in two-dimensional block sizes expressed as a cross-sectional area (m²). NAC pixel scale
100 ranged from 50 – 175 cm/pixel, with size measurement uncertainties on the order of 1 pixel.
101 Blocks with diameters that are approaching the pixel scale or affected by shadows are not
102 included in our analysis because their shape cannot be fully distinguished. The minimum
103 block size measured in this study is ~0.8 m², and the maximum block size measured is
104 ~125 m². A quartile analysis, in particular using the value of the third quartile (Q₃, 75% of
105 observations are smaller than this value), is used to describe trends in block size.

106 **3. Observations**

107 *3.1 Location*

108 The location of blocky wrinkle ridges for eight maria are shown in Figure 2A, B.
109 Although not included in this study, blocky wrinkle ridges are also observed in basalts in
110 Aitken and Grimaldi craters and Maria Cognitum, Humboldtianum, Humorum, Imbrium,

111 Marginis, Moscoviense, Nectaris, Orientale, Smythii, Spumans, and Undarum. Blocky
112 wrinkle ridges are not observed in Maria Anguis, Ingenii, and Insularum, either because
113 wrinkle ridges aren't present and/or there is not enough high resolution imagery to observe
114 blocks.

115 For a given mare in this study, at least 74% of the ridge segment population (the
116 total number of segments digitized to represent the ridges as polylines) examined have
117 block fields (red wrinkle ridge segments in Fig. 3A, B) and the percentage can be as high
118 as 96%, although some number of these segments are unclassified (yellow segments) or
119 non-blocky (cyan segments) (see Methods for color description). Conversely, non-blocky
120 ridge segments represent up to 11% of the population examined, while up to 20% of ridge
121 segments are unclassified. Of the non-blocky segments, 48 – 87% in each mare are affected
122 by craters, either near crater rims if found within a crater, on an ejecta blanket, or in a field
123 of secondary craters.

124 *3.2 Block Field Morphometry*

125 3.2.1 Block Density

126 Block density as a function of local maximum slope is shown in Fig. 4 and ranges
127 from 3 – 82 blocks across 5 – 40° slopes. It should be noted that the reported values of
128 block density are limited to counts of blocks large enough to be resolved in LROC NAC
129 images. Generally, block density (mean and median) increases as slope increases, but there
130 is some variability. First, 7.5° (5° to 10° bin) slopes do not follow this general trend and
131 have a much greater quartile spread than 15° (10° to 20° bin), 25° (20° to 30° bin), and 35°
132 (30° to 40° bin) slopes. Slopes between 30° to 40° also have a large quartile spread, but

133 this could be a function of the small sample size due to a scarcity of slopes in this range
134 along wrinkle ridges. The most common slopes in the wrinkle ridge DEMs are between
135 10° to 20° and have the largest range of block densities. Some data limitations were
136 encountered: A portion of the blocks in Australe, Fecunditatis and Tranquillitatis could not
137 be accurately measured because their size is near the NAC image resolution (50 – 175
138 cm/pixel), and shadows cast by some blocks in Crisium obscuring a portion of a block were
139 not included in this analysis.

140 Increasing average block density with increasing slope holds true for all maria
141 except for a few cases; in Australe (the block density in the 7.5° slope bin is higher than in
142 15° slope bin) and in Crisium (the block density in the 25° slope bin is lower than at 15°
143 slope bin) (Table 1). Six of the ten ridges studied only had 1 – 4 block fields across all
144 slopes where blocks could be counted, while the other 4 ridges had >16 patches across all
145 slopes. Additionally, block density appears to vary widely between ridges within the same
146 mare (Fecunditatis and North Procellarum; Table 1).

147 3.2.2 Block Size

148 The two-dimensional size (cross-sectional area) of blocks observed along wrinkle
149 ridge slopes can be extremely variable across and within maria. However, some trends can
150 be recognized. For slopes of 5° to 10° (7.5° bin) where blocks are present (Fig. 5), 75% of
151 the blocks in each maria (3 mare, one ridge in each) are $\leq \sim 15 \text{ m}^2$ (i.e., $Q_3 \leq \sim 15 \text{ m}^2$). The
152 same is true for slopes of 10° to 20° (15° bin) (Fig. 6; 7 mare, one ridge in each) with the
153 exception of Serenitatis with a $Q_3 \leq \sim 35 \text{ m}^2$ and Frigoris with $Q_3 \leq \sim 57 \text{ m}^2$. Five of the
154 eight ridges with slopes between 20° to 30° (25° bin) (Fig. 7) also have 75% of blocks \leq

155 ~11 m², but 75% of blocks in Tranquillitatis, Frigoris, and Serenitatis are as large as ~30
156 m², ~31 m², and ~25 m², respectively, and have a much larger quartile spread than for other
157 slopes or ridges. Finally, three ridges with blocks along slopes of 30° to 40° (35° bin) (Fig.
158 8) all have 75% of blocks ≤ ~11 m².

159 Figure 9 shows a compilation of all measurements of two-dimensional block size
160 for each ridge (and thus location), showing that 75% of blocks along 6 out of 10 ridges are
161 ≤ ~12 m² for all relevant slopes. The other four ridges have Q₃ ≤ 35 m². The maximum
162 block size across all maria is less than 125 m². For Australe, although 75% of the blocks
163 are ≤ ~9 m² across all slopes, larger blocks are observed with a maximum size of ~41 m².
164 Block sizes in Crisium are fairly consistent across all slopes (Q₃ ≤ ~10 m²) with a maximum
165 block size of ~67 m². While block sizes along Fecunditatis (1) are also fairly consistent (Q₃
166 ≤ ~7 m², with a maximum of ~23 m²), blocks along Fecunditatis (2) are much more variable
167 (Q₃ ≤ ~31 m², with a maximum of ~95 m²). This could be the result of a small sample size
168 for Fecunditatis (2), or suggestive of how the blocks were formed. Blocks along two ridges
169 in North Procellarum (Dorsum Harding and Dorsum Herodotus) are much more similar,
170 although this may be due to the smaller sample size at Herodotus: 75% of blocks at Harding
171 are ≤ ~10 m² with a maximum of ~55 m², while 75% of blocks at Herodotus are ≤ ~12 m²
172 with a maximum of 25 m². Block sizes in Frigoris are the most variable with a minimum
173 of ~3 m² and a maximum of 87 m² and a Q₃ of ~35 m². Despite this variability, the total
174 range of sizes is similar to those observed in other maria. Blocks in Nubium have a Q₃ ≤
175 ~8 m² and a maximum of 11 m². In Serenitatis, 75% of the blocks are ≤ ~28 m² and all
176 blocks are smaller than ~125 m² (the maximum across all maria). Blocks along slopes of

177 wrinkle ridges in Tranquillitatis are smaller than $\sim 92 \text{ m}^2$ with $Q_3 \leq \sim 30 \text{ m}^2$. If we instead
178 look at block size as a function of slope (Fig. 10) without separating by location, we see
179 the maximum block size (and range) is found at 20 to 30° slopes. Additionally, 75% of all
180 blocks for each slope value – regardless of location – are less than $\leq \sim 14 \text{ m}^2$.

181 In addition to block cross-sectional area, a sample of larger, crisper block widths
182 and lengths were selected for one ridge in eight of the mare in this study. Of those blocks,
183 all lengths are less than $\sim 14 \text{ m}$ but are more commonly between $\sim 2 - 8 \text{ m}$ ($l_{avg} = \sim 7 \text{ m}$, σ_l
184 $= 3 \text{ m}$), while block widths are less than 10 m but more commonly between $\sim 1 - 6 \text{ m}$ (w_{avg}
185 $= \sim 4 \text{ m}$, $\sigma_w = 2 \text{ m}$) (Fig. 11). Lines of two-dimensional sphericity ($s = W/L$; Folk, 1974) are
186 plotted on Fig. 11 and show that most block sphericity ranges from $0.5 < s < 1$ ($s_{average} =$
187 0.67). There also seems to be a moderately strong linear relationship between block width
188 and length, with a least squares regression (or “goodness of fit,” R^2) value of 0.72 , meaning
189 that 72% of the variation in width can be explained by length.

190 The analysis of DEMs derived from NAC stereo pairs yields a few general
191 observations: (1) the highest abundance of blocks occurs along slopes of 20° and 30°, (2)
192 blocks are commonly exposed along 15° slopes, and (3) blocks are less common along 10°
193 and 40° slopes. Blocks and high reflectance material are very rarely or not observed on
194 flat ($\leq 5^\circ$ slope) surfaces. The steepest slopes associated with wrinkle ridges are generally
195 found on the vergent side of ridges. The block fields examined are often, but not
196 exclusively, located on the slopes of the vergent side of ridges (Fig. 1, 12).

197 **4. Discussion**

198 The correlation between the location of block fields and areas of steep slope on a
199 wrinkle ridge (examples in Fig. 1, 12) allows one formation hypotheses to be ruled out.
200 Hypothesis 1 (transport) can be eliminated because it would suggest either isolated pockets
201 of blocks traceable to a crater or a continual ray of blocks; neither is observed. We would
202 not expect to see a strong correlation with ridge slope and block fields that follow the trace
203 of the wrinkle ridge. Hypothesis 2 (blocks present before being exposed on wrinkle ridges),
204 however, cannot be ruled out strictly on the basis of preferential locations (spatial
205 correlation of blocks with slope) along wrinkle ridges. It could be argued that if block
206 exposure is controlled solely by surface slope, similar fields of blocks would be expected
207 elsewhere in the maria unassociated with wrinkle ridges. However, wrinkle ridges account
208 for most of the positive relief landforms in the mare other than impact craters. Preexisting
209 blocks may be exposed by downslope movement of regolith triggered by unrelated tectonic
210 or other shallow seismic events.

211 Another possibility (Hypothesis 3), based on the location and correlation of blocks
212 with slope along wrinkle ridges, is that blocks from mare basalts are being formed and
213 exposed by ongoing deformation related to ridge formation. Bending stresses from continued
214 contractional deformation of mare basalts [see Watters, 1988] would be expected to
215 generate fresh blocks. Additionally, the shape of some block fields could be explained by
216 downslope movement of material on steeper slopes. This hypothesis is supported by the
217 observation of blocks seemingly being eroded from outcrop ledges in multiple maria (Fig.
218 13) with blocks observed downslope of those outcrops.

219 The stability of blocks on the lunar surface is an important constraint on the timing
220 of the formation of the block fields. Basilevsky et al. [2013] found that the median survival
221 time of blocks ≥ 2 m against collisional disruption on the surface of the Moon is $\sim 40 - 80$
222 My (with virtually all blocks destroyed in 150 – 300 Ma and larger (10 – 20 m) blocks
223 destroyed more rapidly), suggesting young formation ages of these blocks. Another line of
224 evidence for young formation ages comes from the common association of high reflectance
225 material with blocks. Freshly exposed soil will darken with time as it is exposed to solar
226 wind, cosmic rays, and micrometeoroid impacts, and it has been shown that soil optical
227 maturity matches maximum maturity at the Copernican-Eratosthenian boundary (~ 800 Ma)
228 [Matson et al., 1977; Lucey et al., 2000]. However, impact craters with a wide range of
229 ages exhibit optically immature soil along steep slopes of the crater wall, indicating that
230 downslope movement along the wall mixes and freshens the soil [Grier et al., 2001]. Thus,
231 the common association of high reflectance material with blocks also supports young
232 formation ages of the block fields, as it is likely the regolith that is freshened by downslope
233 movement along steep ridge slopes and possibly from the breakdown of the blocks
234 themselves.

235 Formation of the block fields by downslope movement could be due to seismic
236 shaking from impacts and/or recent tectonic activity along the ridge-forming faults. Mare
237 wrinkle ridges are ancient. Embayment relations between mare basalt flows and wrinkle
238 ridges, along with Apollo Lunar Sounder Experiment (ALSE) data showing evidence of
239 thinning of flows on apparent structural relief [Maxwell, 1978], indicate that ridge
240 formation initiated soon after and continued during emplacement of the mare basalts [see

241 Watters, 1988]. Mare volcanism is estimated to have initiated ~ 4 Ga ago with the largest
242 pulse occurring ~ 3.2 Ga ago [Hiesinger et al., 2000, 2003]. Crater counts for typical
243 wrinkle ridges give an average age of 3.1 to 3.5 Ga [Yue et al., 2017]. The youngest mare
244 basalts estimated to be ~ 1.2 Ga old [Hiesinger et al., 2003] are deformed by wrinkle ridges
245 suggesting that some mare-related crustal shortening continued until relatively recently
246 [Watters and Johnson, 2010]. Recent studies have placed tectonic activity – including
247 faults that form mare wrinkle ridges – as recently as ~ 40 Ma, throughout the Copernican
248 (last ~ 800 Ma) [Watters et al., 2010, 2012; French et al., 2015; van der Bogert et al., 2018;
249 Williams et al., 2019]. Newly established links between lobate thrust fault scarps and
250 shallow moonquakes recorded by the Apollo seismometers suggest current tectonic activity
251 [Watters et al., 2019]. Young wrinkle ridges associated with ridge-scarp transitions may
252 indicate current activity extends to the mare [Williams et al., 2019]. However, boulder
253 falls and tracks are rare near wrinkle ridge block fields suggesting that the cohesive strength
254 of blocks may be limited because the mare basalts are expected to be heavily jointed and
255 fractured and basalt blocks may lose cohesion during a fall.

256 Blocks can occur along wrinkle ridge slopes because as slip on ridge-forming thrust
257 faults continues, layers (such as those in multi-layer mare basalts) bend and buckle.
258 Flexural bending of these mechanical layers may form blocks that further break down into
259 blocks exposed at the surface (in the presence of a thin regolith layer). Block dimension as
260 a function of slope is generally less than ~ 22 m², while dimension as a function of location
261 is generally less than ~ 35 m². This suggests that location rather than slope is a stronger
262 control on block size. This regional variation in the maximum block size could be a result

263 of (for example) thicker basalt flows, younger blocks, or differences in ridge morphology
264 (e.g., slope gradient, or curvature, which is an expression on the contractional strain and
265 the bending stresses acting on the basalt layers). Overall, block size is related to (1)
266 exposure to weathering processes, (2) the mechanical properties of the source material, and
267 (3) the forces acting on the source material. Source material for all blocks is mare basalt,
268 so block size could be a function of how the multi-layered basalt is responding to the
269 contractional strain induced by the slip of the fault. The similarity in block size across eight
270 different maria may be due to cooling joints controlled by the cooling rate and thermal
271 gradient of the lava flow (e.g., Grossenbacher and McDuffie, 1995). Jointing has been
272 observed in most basalt outcrops along Hadley rille on the Moon [Howard et al., 1972]
273 where columnar jointing was also noted, in particular the observation of a block that was
274 bounded by columnar joints (however this seems to be a rare occurrence). Columnar
275 jointing has also been directly observed in HiRISE (High Resolution Imaging Science
276 Experiment) images in the walls of impact craters on Mars [Milazzo et al., 2009].

277 Blocks have been observed and studied along the slopes of Hadley rille at the
278 Apollo 15 landing site. Howard et al. [1972] measured blocks to be between ~10 – 18 m
279 across and jointing was also observed in outcrops near the top of the rille, particularly in
280 the massive mare basalt units. This, along with the observation that the largest blocks are
281 about the same size as the thickness of the unbroken outcrops, led to the conclusion that
282 the most likely source of the blocks is the mare basalt near the top of the rille.

283 Howard et al. [1972] suggest that the maximum size of the blocks at Hadley rille
284 can potentially estimate the minimum thickness of the source layer since some of the

285 outcrops were obscured. We are assuming that blocks are also eroding from outcrop ledges
286 along wrinkle ridges, so we apply the same estimation for layer thickness. The maximum
287 length of all blocks measured in this study (based on the cross-sectional area in LROC
288 NAC images) is ~14 m, but more commonly between ~2 – 8 m ($l_{avg} = \sim 7$ m, $\sigma_l = 3$ m). If
289 we use maximum block lengths in each mare to estimate minimum layer thickness, we get
290 ~7 m for Australe, ~14 m for Crisium, ~6 m for Fecunditatis, ~9 m for Frigoris, ~6 m for
291 North Procellarum, ~7 m for Nubium, ~13 m for Serenitatis, and ~10 m for Tranquillitatis.
292 This assumes the largest blocks are generally representative of the flow thickness where
293 and when blocks were formed by break-up of flows by bending stresses. Because it is likely
294 that blocks, once exposed, will fragment to some degree due to impacts, it must also be
295 assumed that estimates of flow thickness will be minimum values. Variations in flow
296 thickness are expected depending on location within the mare (e.g., thinning effects near
297 the mare edge or along structural relief of wrinkle ridges that existed prior to flow
298 emplacement [Maxwell, 1978; Watters, 1988]): the Frigoris, Nubium, and Serenitatis
299 ridges measured are all less than ~10 km from features that could influence the flow
300 thickness (mare edge or highland outcrop). The Australe, Crisium, and Tranquillitatis
301 ridges are between ~26 – 70 km from an obstructive feature, and the North Procellarum
302 (Harding) and Fecunditatis ridges are greater than ~170 km from an obstructive feature.
303 There does not appear to be a correlation between minimum flow thickness estimates (see
304 above) and distance from flow-obstructive features, so any thinning effects would be from
305 buried features (which are difficult to discern without subsurface imaging).

306 Flow thickness of mare basalts have been estimated by a number of different
307 methods. In particular, the high resolution of LROC NAC images has unequivocally
308 revealed mare basalt layer thicknesses exposed along the walls of craters, pits, and rilles.
309 Robinson et al. [2012] used direct imaging of basalt layers in the walls of craters and pits
310 in the maria to estimate layer thicknesses. The walls of at least 12 craters reveal mare basalt
311 flow thicknesses ranging from 2 – 5 m, and pit walls reveal flow thicknesses ranging from
312 5 – 11 m in Mare Ingenii, 3 – 14 m in Mare Tranquillitatis, and 4 – 12 m in the Marius
313 Hills (Southern Oceanus Procellarum). Enns and Robinson (2013) used LROC NAC
314 images to identify and measure thicknesses of basalt flows exposed in the walls of 50 fresh
315 craters across the maria, resulting in maximum flow thicknesses ranging from 6 – 25 m.
316 As discussed in the previous paragraphs, Howard et al. [1972] estimated ~10 – 18 m thick
317 basalt flows by measuring block sizes exposed along the walls of Hadley rille (Mare
318 Imbrium). Hiesinger et al. [2002] analyzed the shape of crater size-frequency distribution
319 (CSFD) curves and found that a characteristic “knee” in the curves represents two flow
320 units, of which the thicknesses can be determined. They found that, for seven mare basins,
321 flow thicknesses range from ~20 – 220 m with an average of ~30 – 60 m. Gifford and El-
322 Baz [1981] analyzed low-sun photographs for flow front shadows to determine flow
323 thicknesses of surface units, ranging from 1 – 96 m with an average thickness of ~21 m.
324 Thin mare basalt flows no thicker than ~8 to 10 m were suggested by Brett [1975] based
325 on chemical kinetic data from mineral equilibria in lunar samples to estimate cooling rates.

326 Despite the trend of increasing block density with increasing slope, we observe a
327 large range in densities of blocks that occur in patches (Fig. 2, 4). These patches could be

328 influenced by a number of factors: slope (from the observations presented here, more
329 blocks are exposed on steeper slopes), slope gradient (a higher gradient suggests a higher
330 degree of flexural bending, resulting in more blocks), continuity of slope (a small area of
331 large slope won't expose as many blocks as a large area), variability in regolith thickness
332 (blocks are exposed more in areas with thinner regolith [Wilcox et al., 2005]), variability
333 in mare basalt layer thickness (thin layers break more readily and result in smaller, possibly
334 more blocks but below NAC resolution), and mechanical properties of mare basalt (jointed
335 and heavily fractured basalt will generate blocks more easily). Other factors to consider are
336 the mechanical properties and thickness of interbeds (regolith, etc.) in basalt layers. Our
337 analysis shows that block density increases significantly with increasing slope (see Fig. 3),
338 suggesting that slope is an important factor in controlling the location of fields and their
339 block density.

340 **5. Conclusion**

341 We observed block fields throughout the maria on the slopes of wrinkle ridges.
342 Comparisons of NAC imagery with corresponding slope maps indicate that block density
343 increases with increasing slope and blocks are preferentially exposed along wrinkle ridge
344 slopes ranging from 20 – 30°. Block fields may result from seismic shaking due to shallow
345 moonquakes generated by impacts or tectonic activity unrelated to wrinkle ridges, or recent
346 tectonic activity on wrinkle ridge-forming thrust faults. Evidence suggests that young
347 lobate thrust fault scarps and thrust faults that form some mare wrinkle ridges have been
348 active throughout the Copernican (the last ~800 Ma) and as recently as ~40 Ma [Watters
349 et al., 2010, 2012; French et al., 2015; van der Bogert et al., 2018; Williams et al., 2019].

350 Links between lobate thrust fault scarps and shallow moonquakes recorded by the Apollo
351 seismometers suggest current tectonic activity [Watters et al., 2019], and young ridges
352 associated with wrinkle ridge-lobate scarp transitions suggests some current activity in the
353 nearside mare [Williams et al., 2019]. Recent activity agrees well with collision disruption
354 rates of meter-scale blocks (between $\sim 40 - 300$ Ma) [Basilevsky et al., 2013] and the
355 common association of high reflectance material representing fresher, “immature” soils.

356 The 1,368 blocks measured in the study have a median cross-sectional area of ~ 7
357 m^2 , a mean $\sim 12 \text{ m}^2$, a standard deviation $\sim 13 \text{ m}^2$, and 75% (Q_3) of the measured blocks are
358 $\leq \sim 14 \text{ m}^2$. The largest variation in cross-sectional area of the blocks is found with location
359 and not as a function of the slope, suggesting that location rather than slope is a stronger
360 control on block size. Blocks measured for this study are no longer than 14 m (commonly
361 2 – 8 m) and no wider than ~ 10 m (commonly 1 – 6 m), and most blocks have a two-
362 dimensional sphericity ranging from $0.5 < S < 1$ ($S_{\text{average}} = 0.67$). If the maximum size of
363 blocks is controlled by the minimum layer thickness or joint width, basalt flows ranging
364 from $\sim 2 - 14$ m thick agree very well with previous mare basalt layer thickness estimates
365 [Brett, 1975; Gifford and El-Baz, 1981; Hiesinger et al., 2016].

366 Block density could be controlled by a number of factors including slope, slope
367 gradient and continuity, regolith and interlayer thickness, and basalt thickness and
368 mechanical properties. Results presented here show that slope is an important controlling
369 factor. It is uncertain at this time to what degree each of the other factors play in generating
370 block fields.

371 **Acknowledgements**

372 We wish to thank Ernst Hauber and an anonymous reviewer for insightful comments and
373 suggestions that greatly improved the paper. This work would not have been possible
374 without the dedication and hard work of the LROC team, not only in data acquisition and
375 distribution but in support as well. Groups at ASU and UA are responsible for
376 processing of NAC stereo pairs to DEMs, data that is the backbone of this work. We
377 gratefully acknowledge the LRO engineers and technical support personnel.
378 This work was supported by the LRO Project and an ASU LROC Contract (TRW). Data
379 are available on the Smithsonian's Figshare site
380 (<https://dx.doi.org/10.25573/data.9955277>).

381

382

383 **References**

384 Anderson, J.A., Sides, S.C., Soltesz, D.L., Sucharski, T.L., & Becker, K.J. (2004).
385 Modernization of the Integrated Software for Imagers and Spectrometers. 35th Lunar and
386 Planetary Science Conference, Abstract #2039.

387

388 Basilevsky, A.T., Head, J.W., & Horz, F. (2013). Survival times of meter-sized blocks on
389 the surface of the Moon. *Planetary and Space Science*, 89, 118-126.
390 <https://doi.org/10.1016/j.pss.2013.07.011>

391

392 Brett, R. (1975). Thicknesses of some lunar mare basalt flows and ejecta blankets based on
393 chemical kinetic data. *Geochimica et Cosmochimica Acta*, 39, 1135-1141.
394 [https://doi.org/10.1016/0016-7037\(75\)90055-1](https://doi.org/10.1016/0016-7037(75)90055-1)

395

396 Burns, K. N., Speyerer, E. J., Robinson, M. S., Tran, T., Rosiek, M. R., Archinal, B. A.,
397 Howington-Kraus, E., & the LROC Science Team (2012). Digital Elevation Models and
398 Derived Products from LROC NAC Stereo Observations. International Archives of the
399 Photogrammetry, Remote Sensing, and Spatial Information Sciences XXXIX-B4, 483-
400 488. doi:10.5194/isprsarchives-XXXIX-B4-483-2012

401

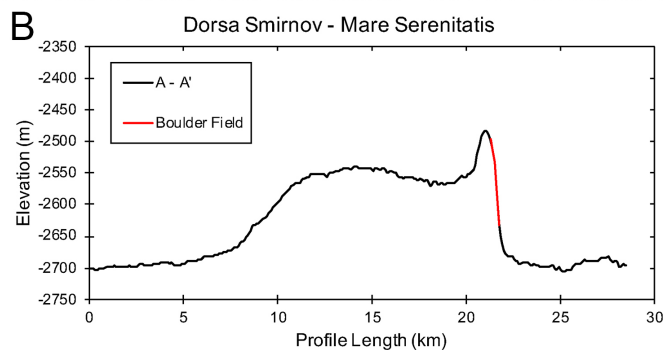
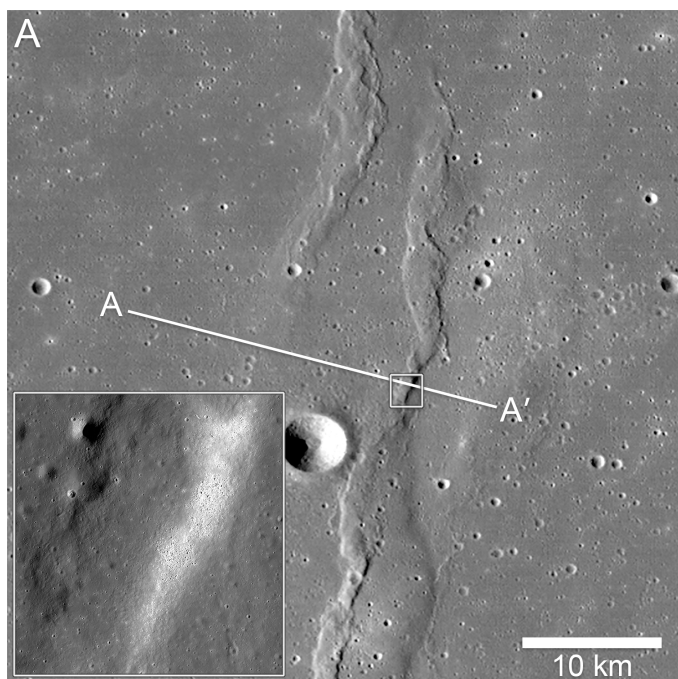
402 Enns, A.C., & Robinson, M.S. (2013). Basaltic Layers Exposed in Lunar Mare Craters.
403 44th Lunar and Planetary Science Conference, Abstract #2751.

404

- 405 Folk, R. L. (1974). Petrology of Sedimentary Rocks. Hemphill, Austin, Texas.
406
- 407 French, R.A., Bina, C.R., Robinson, M.S., & Watters, T.R. (2015). Small-scale lunar
408 graben: Distribution, dimensions, and formation processes. *Icarus*, 252, 95-106.
409 <https://doi.org/10.1016/j.icarus.2014.12.031>
410
- 411 Gifford, A.W., & El-Baz, F. (1981). Thicknesses of Lunar Mare Flow Fronts. *The Moon*
412 *and the Planets*, 24, 391-398. <https://doi.org/10.1007/BF00896904>
413
- 414 Grier, J.A., McEwan, A.S., Lucey, P.G., Milazzo, M., & Strom, R.G. (2001). Optical
415 maturity of ejecta from large rayed lunar craters. *Journal of Geophysical Research*, 106,
416 32847-32862. <https://doi.org/10.1029/1999JE001160>
417
- 418 Grossenbacher, K.A., & McDuffie, S.M. (1995). Conductive cooling of lava: columnar
419 joint diameter and stria width as functions of cooling rate and thermal gradient. *Journal of*
420 *Volcanology and Geothermal Research*, 69, 95-103. [https://doi.org/10.1016/0377-](https://doi.org/10.1016/0377-0273(95)00032-1)
421 [0273\(95\)00032-1](https://doi.org/10.1016/0377-0273(95)00032-1)
422
- 423 Hiesinger, H., Head, J.W., Wolf, U., Jaumann, R., & Neukum, G. (2002). Lunar mare
424 basalt flow units: Thicknesses determined from crater size-frequency distributions.
425 *Geophysical Research Letters*, 29, 10.1029/2002GL014847.
426 <https://doi.org/10.1029/2002GL014847>
427
- 428 Howard, K.A., Head, J.W., & Swann, G.A. (1972). Geology of Hadley Rille: Preliminary
429 Report. U.S. Department of the Interior Geological Survey, Interagency Report: 41, 1-63.
430
- 431 Howard, K. A., Head, J. W., & Swann, G.A. (1972). Geology of Hadley Rille.
432 Proceedings of the 3rd Lunar and Planetary Science Conference, 1 –14.
433
- 434 Lucey, P.G., Blewett, D.T., Taylor, G.J., & Hawke, B.R. (2000). Imaging of lunar surface
435 maturity. *Journal of Geophysical Research*, 105, 20377-20386.
436 <https://doi.org/10.1029/1999JE001110>
437
- 438 Matson, D.L., Johnson, T.V., & Veeder, G.J. (1977). Soil maturity and planetary regoliths:
439 The Moon, Mercury, and the asteroids. Proceedings of the 8th Lunar Science Conference,
440 1001-1011.
441
- 442 Maxwell, T.A. (1978). Origin of multi-ring basin ridge systems: an upper limit to elastic
443 deformation based on a finite-element model. Proceedings of the 9th Lunar and Planetary
444 Science Conference, 3541-3559.
445
- 446 Milazzo, M.P., Keszthelyi, L.P., Rosiek, M., Mattson, S., Verba, C., Beyer, R.A., Geissler,
447 P.E., McEwan, A.S., & the HiRISE Team (2009). Discovery of columnar jointing on Mars.
448 *Geology*, 37, 171-174. <https://doi.org/10.1130/G25187A.1>

- 449
450 Plescia, J.B. & Golombek, M.P. (1986). Origin of planetary wrinkle ridges based on the
451 study of terrestrial analogs. *GSA Bulletin*, 97, 1289-1299. [https://doi.org/10.1130/0016-](https://doi.org/10.1130/0016-7606(1986)97%3C1289:OOPWRB%3E2.0.CO;2)
452 [7606\(1986\)97%3C1289:OOPWRB%3E2.0.CO;2](https://doi.org/10.1130/0016-7606(1986)97%3C1289:OOPWRB%3E2.0.CO;2)
453
454 Robinson, M.S., Ashley, J.W., Boyd, A.K., Wagner, R.V., Speyerer, E.J., Hawke, B.R.,
455 Hiesinger, H., & van der Bogert, C.H. (2012). Confirmation of sublunarean voids and thin
456 layering in mare deposits. *Planetary and Space Science*, 69, 18-27.
457 <https://doi.org/10.1016/j.pss.2012.05.008>
458
459 Schultz, R.A. (2000). Localization of bedding plane slip and backthrust faults above blind
460 thrust faults: Keys to wrinkle ridge structure. *Journal of Geophysical Research*, 105,
461 12035-12052. <https://doi.org/10.1029/1999JE001212>
462
463 Speyerer, E.J., Robinson, M.S., Denevi, B.W., & LROC Science Team (2011). Lunar
464 Reconnaissance Orbiter Camera Global Morphological Map of the Moon. Lunar and
465 Planetary Science Conference XLII, Abstract #2387.
466
467 Spudis, P.D., Swann, G.A., & Greeley, R. (1988). The formation of Hadley Rille and
468 implications for the geology of the Apollo 15 region. Proceedings of the 18th Lunar
469 Planetary Science Conference, 243–254.
470
471 van der Bogert, C.H., Clark, J.D., Hiesinger, H., Banks, M.E., Watters, T.R. & Robinson,
472 M.S. (2018). How old are lunar lobate scarps? 1. Seismic resetting of the crater size-
473 frequency distribution. *Icarus*, 306, 225-242.
474
475 Watters, T.R. (1988). Wrinkle Ridge Assemblages on the Terrestrial Planets. *Journal of*
476 *Geophysical Research*, 93, 10236-10254. <https://doi.org/10.1029/JB093iB09p10236>
477
478 Watters, T.R., Robinson, M.S., Banks, M.E., Tran, T., & Denevi, B.W. (2012). Recent
479 extensional tectonics on the Moon revealed by the Lunar Reconnaissance Orbiter Camera.
480 *Nature Geoscience*, 5, 181-185.
481
482 Watters, T.R., Robinson, M.S., Beyer, R.A., Banks, M.E., Bell, J.F., Pritchard, M.E.,
483 Hiesinger, H., van der Bogert, C.H., Thomas, P.C., Turtle, E.P., & Williams, N.R. (2010).
484 Evidence of Recent Thrust Faulting on the Moon Revealed by the Lunar Reconnaissance
485 Orbiter Camera. *Science*, 329, 936-940. DOI: 10.1126/science.1189590.
486
487 Watters, T.R., Weber, R.C., Collins, G.C., Howley, I.J., Schmerr, N.C., & Johnson, C.L.
488 (2019) Shallow seismic activity and young thrust faults on the Moon, *Nature Geoscience*,
489 12, 411-417.
490

- 491 Wilcox, B.B., Robinson, M.S., Thomas, P.C., & Hawke, B.R. (2005). Constraints on the
492 depth and variability of the lunar regolith. *Meteoritics & Planetary Science*, 40, 695-710.
493 <https://doi.org/10.1111/j.1945-5100.2005.tb00974.x>
- 494 Williams, N.R., Robinson, M.S., Bell III, J.F., Watters, T.R., Banks, M.E., Daud, K., &
495 French, R.A. (2019). New Views of Tectonism in Mare Frigoris. *Icarus*, 326, 151-161.
496 <https://doi.org/10.1016/j.icarus.2019.03.002>.
- 497 Yue, Z., Michael, G.G., Di, K., & Liu, J. (2017). Global survey of lunar wrinkle ridge
498 formation times. *Earth and Planetary Science Letters*, 477, 14-20.
499



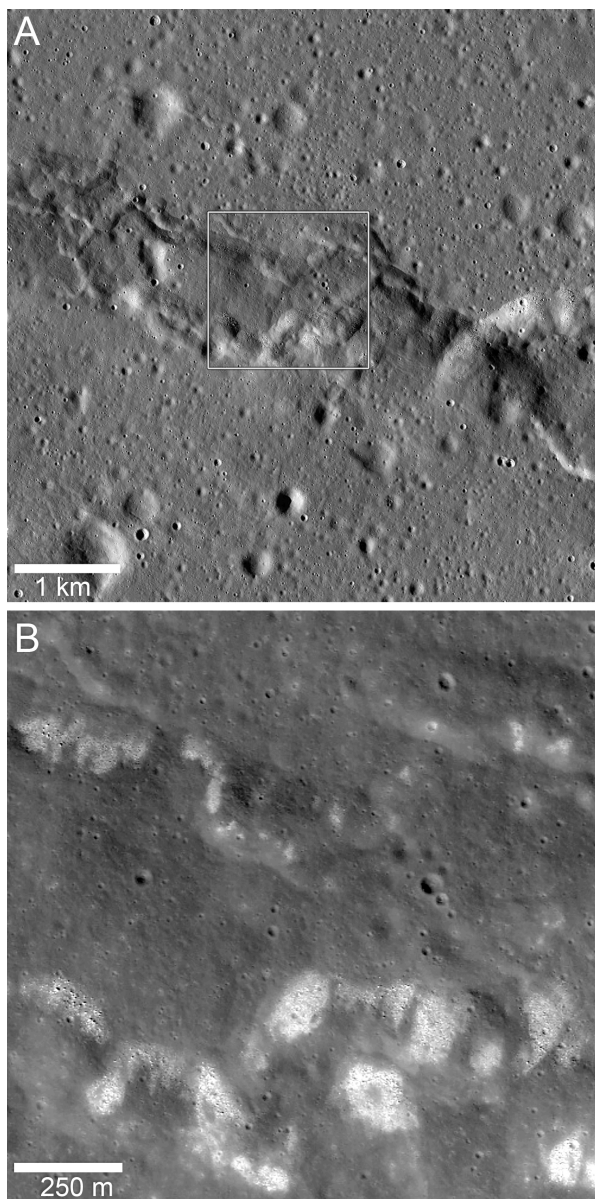
500

501 Figure 1. Typical wrinkle ridges deforming mare basalts. A) LROC WAC mosaic shows
 502 the complex nature of Dorsa Smirnov, a wrinkle ridge in Mare Serenitatis. The small box
 503 indicates the location of a block field associated with the ridge shown the LROC NAC
 504 inset image (frame #1108110462R). B) The topographic profile across Dorsa Smirnov
 505 shows the two primary morphologic elements of wrinkle ridges, a broad arch and a
 506 superimposed relatively narrow ridge. The block field shown in (A) occurs on the
 507 relatively steep slopes of the vergent side of the ridge, indicated by the red line on the
 508 topographic profile. The location of the topographic profile is shown in (A). The profile

509 was extracted from the SLDEM2015 topographic data and elevations are relative to 1737.4

510 reference radius. The vertical exaggeration is ~ 34 .

511



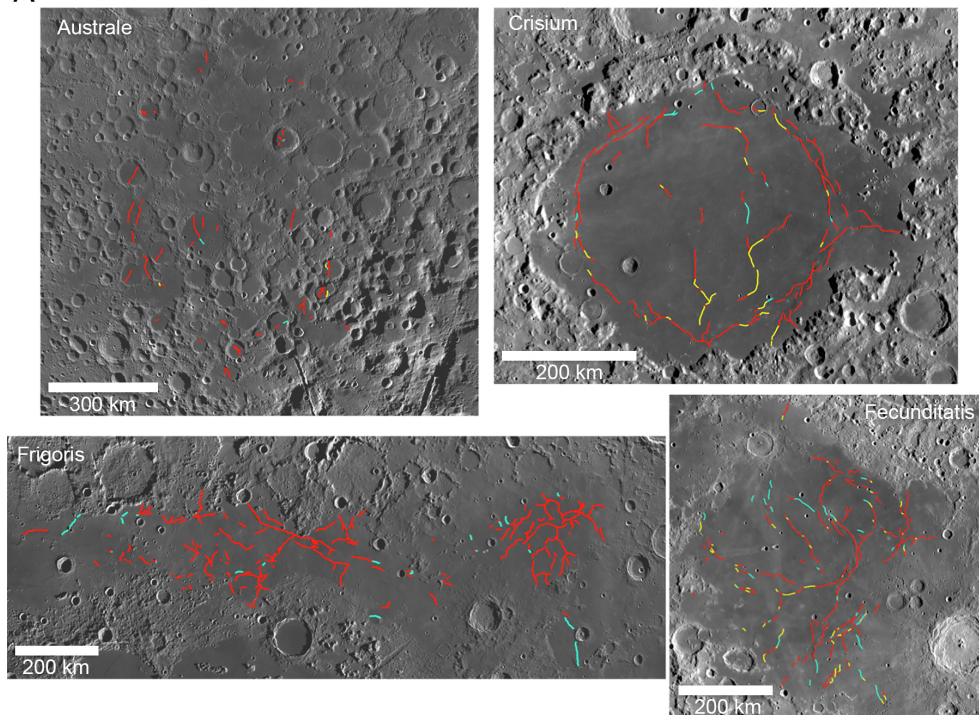
512

513 Figure 2. Wrinkle ridges and block fields. A) A roughly east-west oriented wrinkle ridge

514 located on the western margin of Serenitatis (23.45°N , 8.08°E) is associated with a lobate

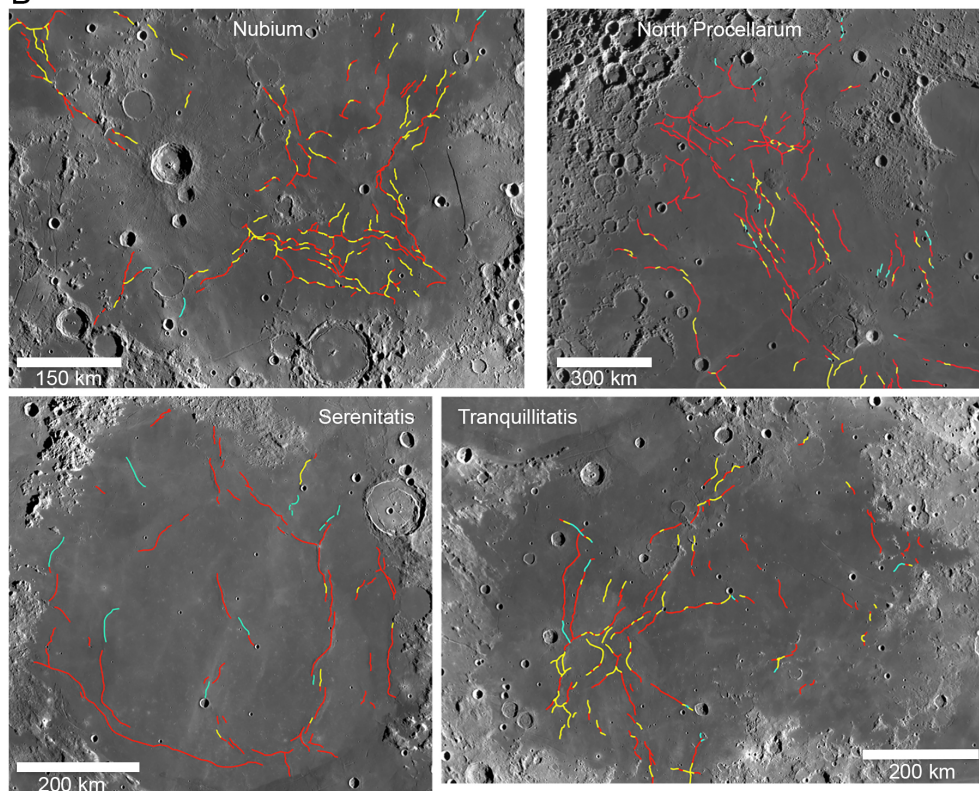
515 scarp transition at the mare-highlands contact [see Watters and Johnson, 2010]. The LROC
516 NAC frame is M1142390360L. B) Blocks and high reflectance material (bright patches)
517 are found along segments of the wrinkle ridge. The boulder fields occur on the north-
518 facing slope of the vergent side of the ridge (north is up). The box in (A) indicates the
519 location of the block fields shown in (B). The LROC NAC frame is M106826896L, spatial
520 resolution of 1.25 m/pixel).

A



521

B

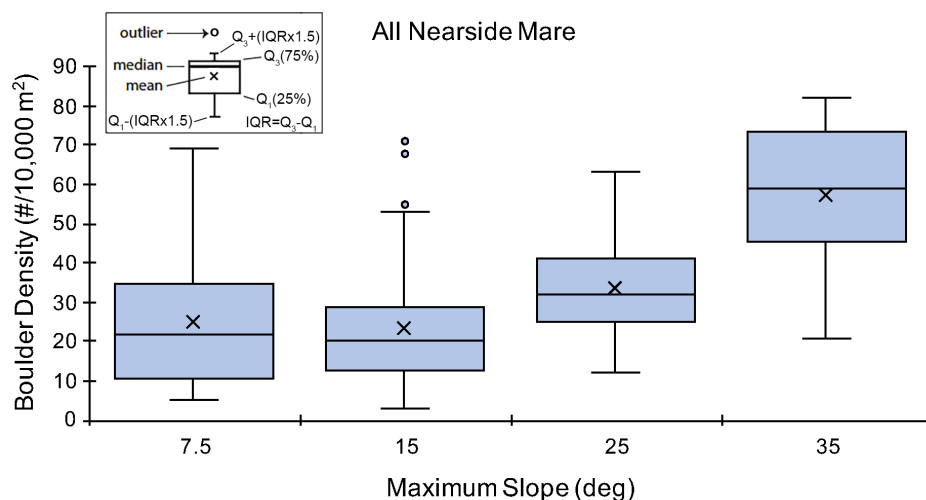


522

523 Figure 3. Wrinkle ridge location maps for the 8 maria selected for this study. A) Locations
 524 of ridges examined in Mare Australe, Crisium, Frigoris, and Fecunditatis. B) Locations of
 525 ridges examined in Mare Nubium, north Procellarum, Serenitatis, and Tranquillitatis. Red
 526 segments are blocky ridges, cyan are non-blocky, and yellow are unclassified. All panel
 527 backgrounds are WAC Global mosaics with native resolution of 100 m/pixel [Speyerer et
 528 al., 2011].

529

530



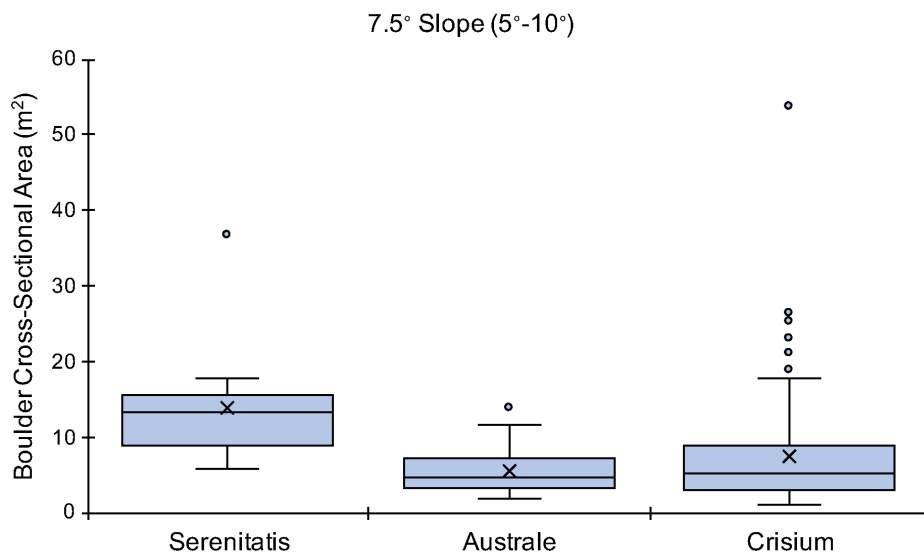
531

532

533 Figure 4. Box and whisker plots of block density (number of blocks per 10,000 m²) as a
 534 function of local maximum ridge slope. The sample range of the 7.5° bin is 5° to 10°, the
 535 15° bin range is 10° to 20°, the 25° bin range is 20° to 30°, and the 35° bin range is 30° to
 536 40° slopes. The upper and lower ends of the boxes represent the third quartile Q₃ (75
 537 percentile) and first quartile Q₁ (25 percentile) respectively, the height of the box is the
 538 interquartile range IQR, the horizontal line is the median and the × is the mean (see inset).

539 The whiskers (the two lines outside the boxes) are equal to the values of Q_1 or $Q_3 \pm$ the
 540 $IQR \times 1.5$; points outside this range are considered outliers mark by circles.

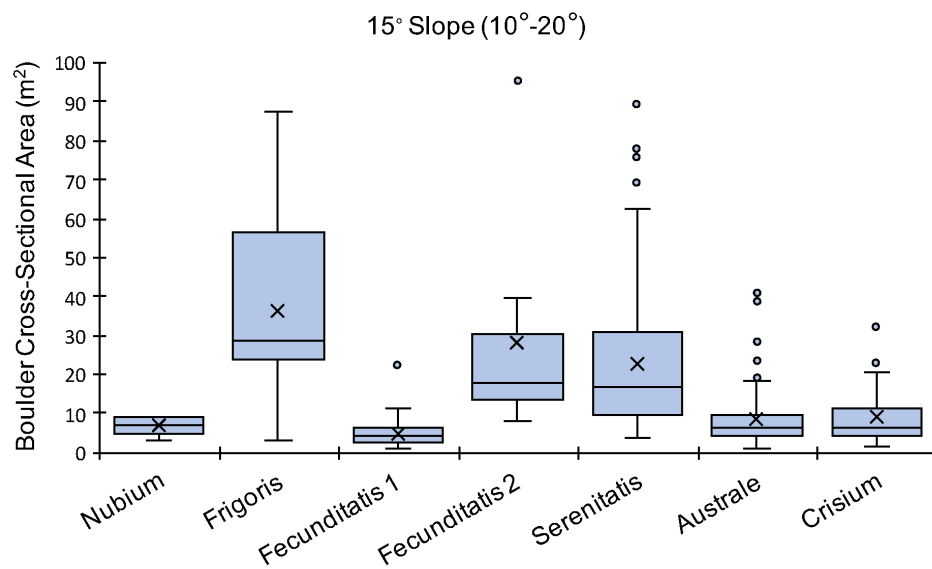
541



542
 543 Figure 5. Box and whisker plots of two-dimensional block size (cross-sectional area in m^2)
 544 for 7.5° ridge slopes. The sample range of slopes for the 7.5° bin is 5° to 10° . See Fig. 3
 545 for explanation of plots.

546

547

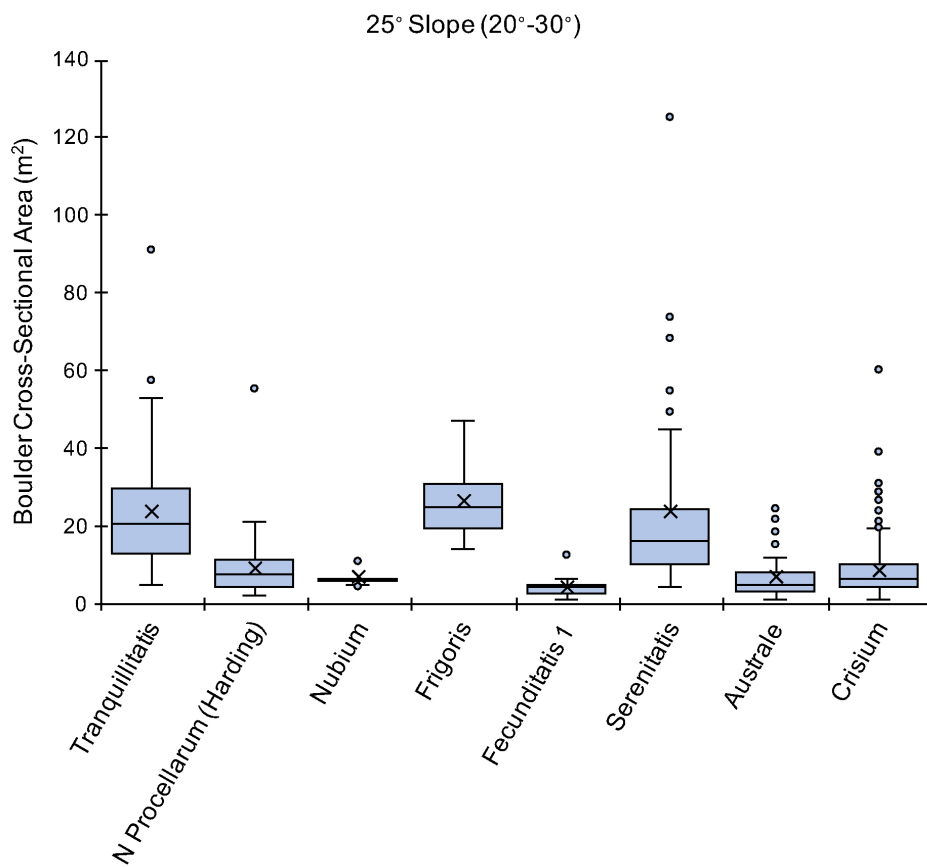


548

549 Figure 6. Box and whisker plots of two-dimensional block size (cross-sectional area in m²)

550 for 15° ridge slopes. The sample range of slopes for the 15° bin is 10° to 20°. See Fig. 3

551 for explanation of plots.

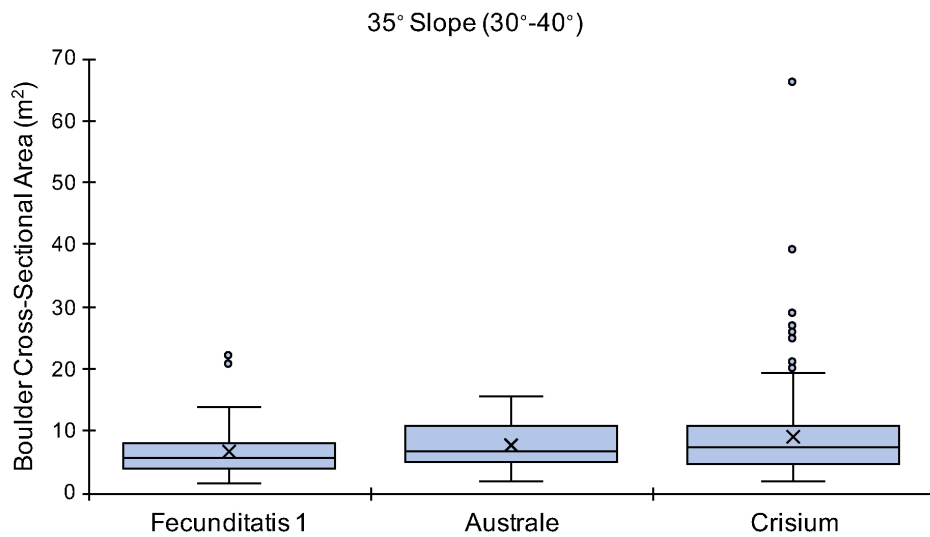


552

553 Figure 7. Box and whisker plots of two-dimensional block size (cross-sectional area in m²)

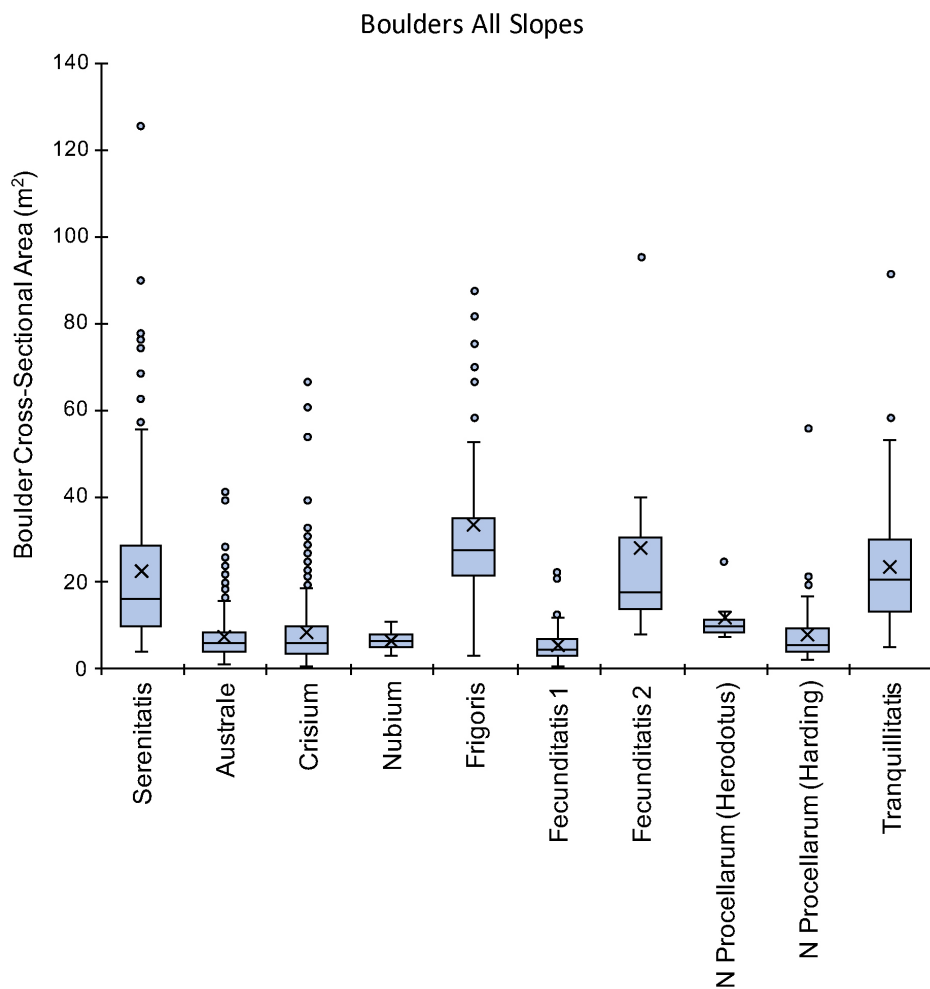
554 for 25° ridge slopes. The sample range of slopes for the 25° bin is 20° to 30°. See Fig. 3

555 for explanation of plots.



556
557

558 Figure 8. Box and whisker plots of two-dimensional block size (cross-sectional area in m²)
559 for 35° ridge slopes. The sample range of slopes for the 35° bin is 30° to 40°. See Fig. 3
560 for explanation of plots.

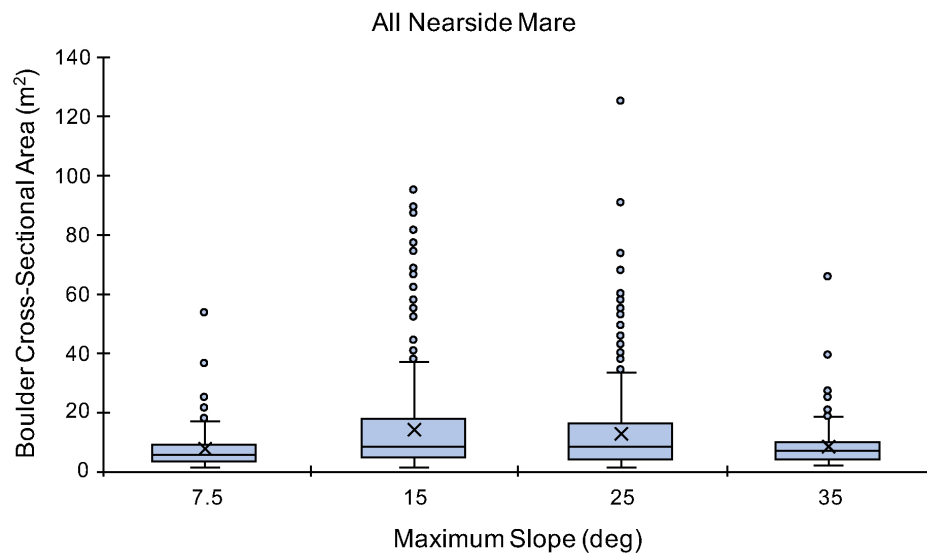


561

562

563 Figure 9. Box and whisker plots of two-dimensional block size (cross-sectional area in m²)

564 by mare. See Fig. 3 for explanation of plots.



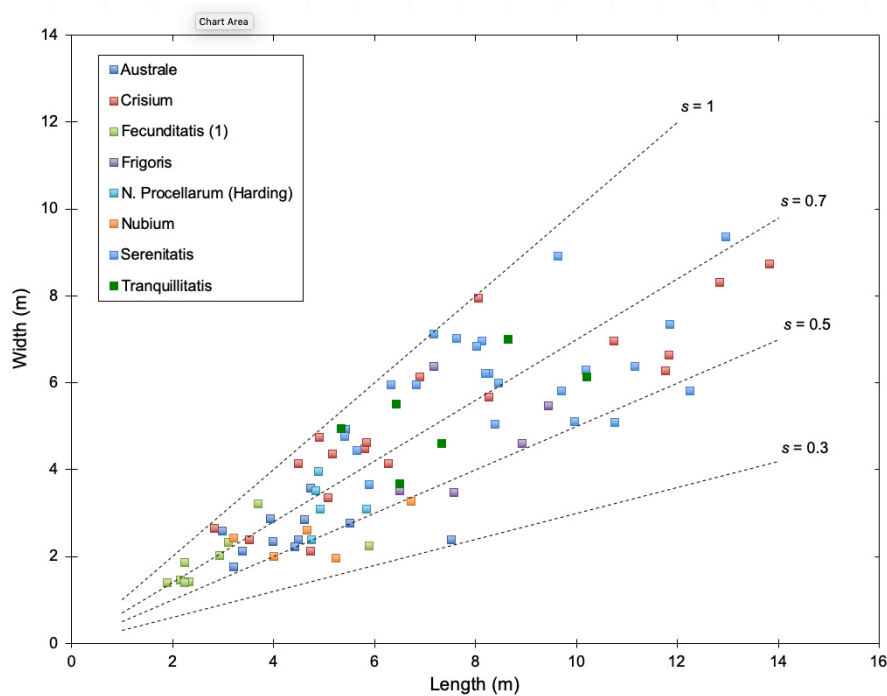
565

566

567 Figure 10. Box and whisker plots of two-dimensional block size (cross-sectional area in

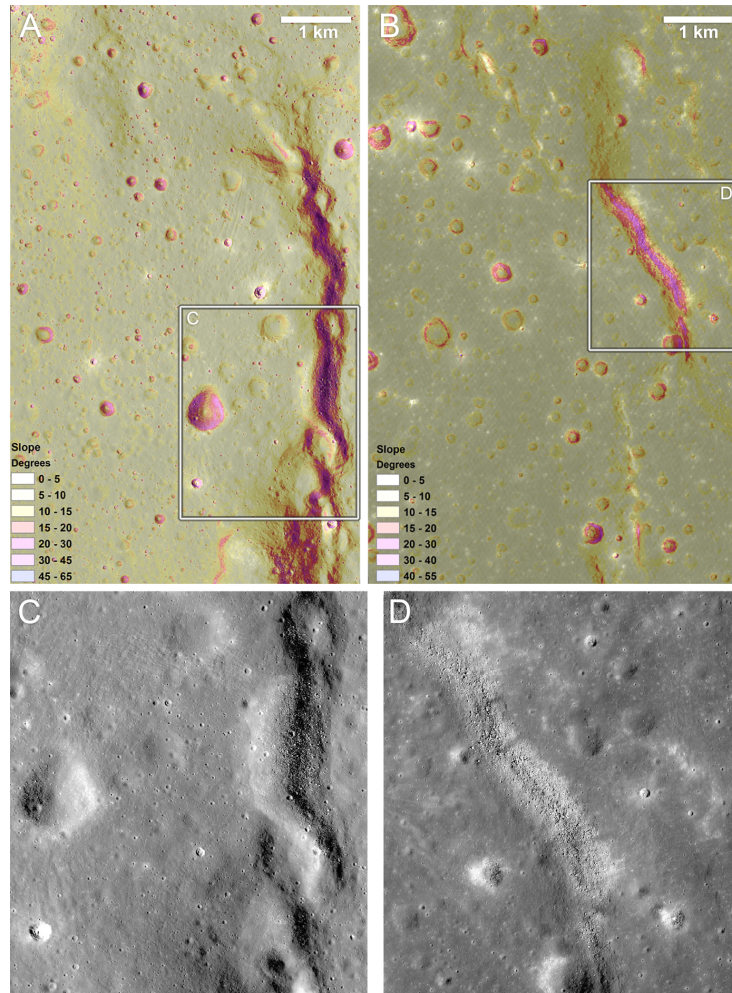
568 m²) as a function of maximum ridge slope. See Fig. 3 for explanation of plots.

569



570

571 Figure 11. Comparing the two-dimensional sphericity ($s = W/L$) of a sample of blocks
 572 across eight ridges in this study, revealing a moderately strong relationship between width
 573 and length ($R^2 = 0.72$).



574

575

576 Figure 12. NAC images overlain by slope maps (generated from DEMs) for segments of

577 Dorsa Tetyaev (A) in Mare Crisium (NAC frame M119435647) and Dorsa Nicol (B) in

578 Mare Serenitatis (NAC frame M1105773947). Slope maps were generated using the

579 *Slope* tool in ArcMap. The tool fits a plane to the DEM values in a 3 x 3 cell

580 neighborhood around the center cell. The area for a given slope value is the square of

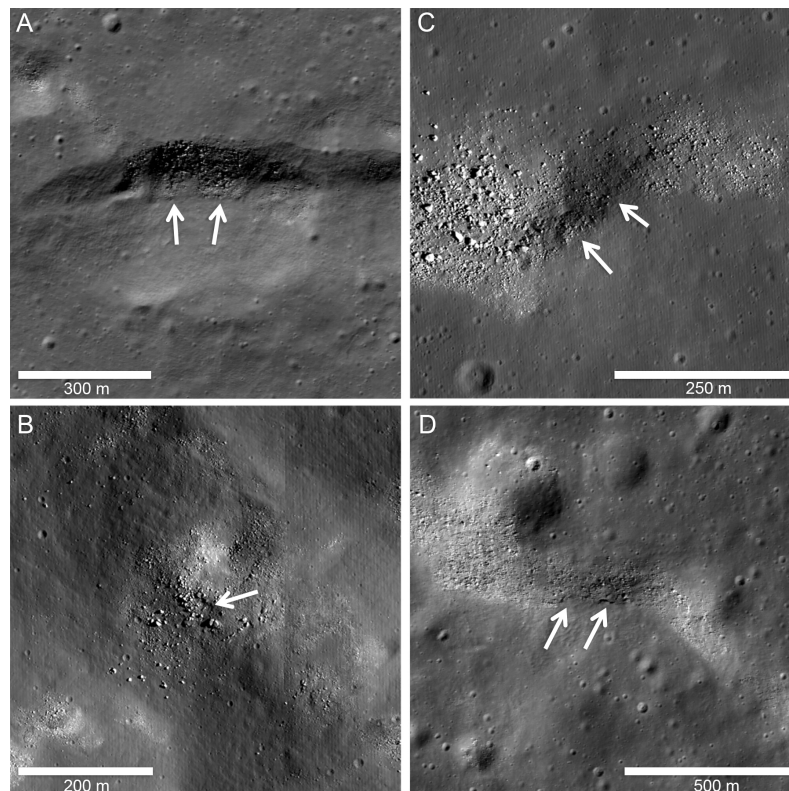
581 DEM spatial resolution. The spatial resolution of the Tetyaev and Nicol DEMs is 2 m

582 and 5 m per pixel, respectively. Inset boxes show the locations of block fields associated

583 with Dorsa Tetyaev (C) and Dorsa Nicol (D) where there are strong correlations between

584 exposed blocks and high slopes.

585



586
587

588 Figure 13. Examples of blocks exposed on wrinkle ridges along apparent outcrop ledges.
589 Wrinkle ridge blocks fields (white arrows) in A) Frigoris (54.03°N , 37.18°E) (image frame
590 M1105666034R, 1.62 m/pixel), B) Serenitatis (19.39°N , 14.94°E) (image frame
591 M113860238L, 0.79 m/pixel), C) Procellarum (11.31°S , 37.87°W) (image frame
592 M160200185R, 0.79 m/pixel), and D) Procellarum (45.99°N , 69.48°W) (image frame
593 M1106366414L, 1.08 m/pixel).

594

595

596

598 **Table 1. Wrinkle Ridge Block Density Data.**

Ridge	Image ID	# of blocks counted	Block Density Range (N/10,000 m ²)	# Density Counts	7.5° Mean Block Density	15° Mean Block Density	25° Mean Block Density	35° Mean Block Density
Australe	M187748539	265	14 - 80	28	32	29	41	62
Crisium	M119435647	514	23 - 82	18	38	59	46	67
Fecunditatis (1)	M150164898	176	10 - 59	16	(18)	23	27	(59)
Fecunditatis (2)	M1107953768	25	12 - 21	2	--	(12)	--	(21)
Frigoris	M1116771628	56	12 - 30	4	--	20	(22)	--
N. Procellarum (Harding)	M173327696	65	3 - 41	3	--	(3)	29	--
N. Procellarum (Herodotus)	M1136889617	7	7	2	(5)	(7)	--	--
Nubium	M183617448	26	4 - 12	3	--	5	(12)	--
Serenitatis	M1105773947	158	3 - 46	44	11	18	30	--
Tranquillitatis	M183274963	76	13	1	--	--	(13)	--

599 The number of density counts represents block density measurements in sample
600 rectangles with areas of 10,000 m² across all slopes for that mare. Values in parentheses
601 are single measurements and values in bold are those that don't follow the trend of
602 increasing density with increasing slope.